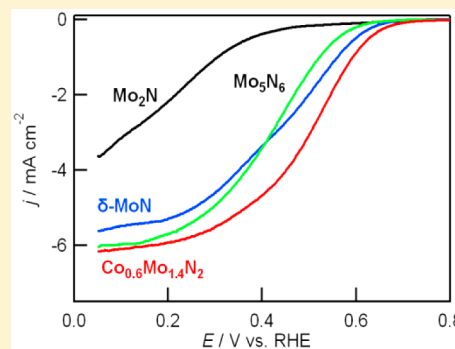


Molybdenum Nitrides as Oxygen Reduction Reaction Catalysts: Structural and Electrochemical Studies

Bingfei Cao,^{†,‡} Joerg C. Neufeind,[§] Radoslav R. Adzic,[‡] and Peter G. Khalifah^{*,†,‡}[†]Chemistry Department, Stony Brook University, Stony Brook, New York 11794, United States[‡]Chemistry Department, Brookhaven National Laboratory, Upton, New York 11793, United States[§]Chemical and Engineering Materials Division, Oak Ridge National Laboratory, Oak Ridge, Tennessee 37831, United States

Supporting Information

ABSTRACT: Monometallic (δ -MoN, Mo₅N₆, and Mo₂N) and bimetallic molybdenum nitrides (Co_{0.6}Mo_{1.4}N₂) were investigated as electrocatalysts for the oxygen reduction reaction (ORR), which is a key half-reaction in hydrogen fuel cells. Monometallic hexagonal molybdenum nitrides are found to exhibit improved activities over rock salt type molybdenum nitride (γ -Mo₂N), suggesting that improvements are due to either the higher molybdenum valence or a more favorable coordination environment in the hexagonal structures. Further enhancements in activity were found for hexagonal bimetallic cobalt molybdenum nitride (Co_{0.6}Mo_{1.4}N₂), resulting in a modest onset potential of 0.713 V versus reversible hydrogen electrode (RHE). Co_{0.6}Mo_{1.4}N₂ exhibits good stability in acidic environments, and in the potential range lower than 0.5 V versus RHE, the ORR appears to proceed via a four-electron mechanism based on the analysis of rotating disc electrode results. A redetermination of the structures of the binary molybdenum nitrides was carried out using neutron diffraction data, which is far more sensitive to nitrogen site positions than X-ray diffraction data. The revised monometallic hexagonal nitride structures all share many common features with the Co_{0.6}Mo_{1.4}N₂ structure, which has alternating layers of cations in octahedral and trigonal prismatic coordination, and are thus not limited to only trigonal prismatic Mo environments (as was originally postulated for δ -MoN).



Efficient and effective electrocatalysts are a key requirement for the development of fuel cells that can generate power from chemical fuels much more efficiently than present internal combustion processes.¹ Hydrogen fuel cells, and in particular polymer electrolyte membrane fuel cells (PEMFCs), can provide high power at low operating temperatures, but they presently suffer substantial performance and cost limitations associated with the challenges of efficiently catalyzing the chemical reactions required for electricity production. In PEMFCs, the most challenging reaction to catalyze is the oxygen reduction reaction (ORR) on the cathode due to the poor kinetics of this four-electron reaction. Because of this, the overpotential on the cathode side of PEMFCs is much larger than that on the anode reaction, where the more facile two-electron oxidation of H₂ to H⁺ occurs. Platinum and platinum-containing alloys are the most widespread and effective cathode catalysts for ORR in PEMFCs.² However, the high cost and tremendous scarcity of platinum remain major obstacles to the commercialization of PEMFCs. The development of alternative non-noble metal catalysts is therefore very important. Transition metal macrocycles, oxides, carbides, and nitrides have been widely investigated for ORR catalysis and provide some of the best alternates, though none of these systems match the activity and stability of Pt under PEMFC operating conditions.^{3–6} Transition metal catalysts in Group 4–5, such as zirconium oxide, titanium nitride, and tantalum oxynitride, have

been shown to have excellent stability in acidic electrolyte, but they exhibit impractically low ORR activities.^{4,6} Under basic conditions, transition metal macrocycles containing Co, Fe, or Cu have shown ORR activities and long-term durabilities comparable to Pt, but these systems do not exhibit the same functionality in acidic environments under which PEMFC are commonly operated due to the solubility of their 3d transition metals.⁵

Transition metal nitrides, as alternatives to Pt for acidic ORR catalysis, have already been demonstrated to exhibit both modest activity and modest stability, and they represent a good system for testing whether the introduction of structural complexity by chemical substitution can lead to further improvements. These nitrides have both low electrical resistance and good corrosion resistance.⁴ The metal–nitrogen bonding at the nitride surface is believed to promote the donation of electrons to oxygen molecules more than for the corresponding oxide analogues, a property that is expected to be favorable for ORR activity. Previously, both MoN and Mo₂N have been demonstrated to exhibit modest ORR activities and to have an ORR pathway that is primarily a four-electron process.^{7–9} Preliminary durability tests showed no decay in performance for Mo₂N (60 h) and MoN (10 h) in 0.5 M

Received: October 10, 2014

Published: February 9, 2015

H₂SO₄ over the time scale of the testing.^{7,8} These monometallic molybdenum nitrides therefore represent a promising starting point for the design of more complex nitrides, which may exhibit enhanced activity and stability relative to their binary counterparts.

In acidic conditions, the previously reported ORR activity of MoN (onset voltage of 0.75 V vs RHE) was higher than that of Mo₂N (0.7 V). Density functional theory studies indicated that the electronic states associated with the MoN hexagonal crystal structure and the favorable local geometry of Mo sites facilitate oxygen adsorption and thus may enhance ORR activity relative to Mo₂N.⁹ It is therefore worthwhile to study a wider range of molybdenum nitrides to better understand the correlation between crystal structure and ORR activity.

Monometallic molybdenum nitrides have been reported to have structures based on simple close-packed geometries. One such compound is cubic Mo₂N, which has a face-centered cubic (fcc) rock salt structure with an ABC repeat sequence of anion layers.¹⁰ The coordination environment of Mo within the rock salt structure would consist of only MoN₆ octahedra if the nitrogen site was fully occupied. However, the nitrogen site is only half-occupied, so it is expected that the Mo cations on average have a coordination number of three, an unusual geometry that is perhaps stabilized by the low average Mo valence of +1.5. Another compound with only octahedral local environments is δ_3 -MoN with the NiAs structure type that has the simple two-layered hexagonal close packed (hcp) stacking of octahedral layers in an AB sequence.¹¹ Although δ_1 -MoN has an X-ray diffraction (XRD) pattern that is nearly indistinguishable from that of δ_3 -MoN, it has been reported to have a structure based on the WC prototype that has only A anion layers, and in which Mo is found exclusively in a trigonal prismatic MoN₆ environment.¹¹ The arrangement of Mo cations in the δ_1 and δ_3 structures are identical, and thus the weak sensitivity of X-rays to N anions makes it nearly impossible to differentiate between these structure models using XRD data.

In contrast to the simple stacking sequences for the above binary molybdenum nitrides, the X-ray diffraction pattern reported for Mo₃N₆ has been indexed in a $\sqrt{3} \times \sqrt{3} \times 4$ superstructure.^{11,12} The strong subcell peaks in the Mo₃N₆ diffraction pattern are very similar to those of δ_1 -MoN, though the weak but clearly resolved superstructure peaks seen in Mo₃N₆ XRD patterns suggest that Mo cations are slightly displaced away from the ideal hexagonal sites in the δ_1 and δ_3 polytypes. Furthermore, the four-layered repeat sequence in the *c*-axis direction suggests that the Mo₃N₆ structure has a mixture of octahedral and prismatic local environments, as has been previously proposed for this compound and closely related compounds such as Fe_{0.8}Mo_{1.2}N₂.^{11–13}

We have recently discovered that the compound Co_{0.6}Mo_{1.4}N₂ has greatly enhanced electrocatalytic activity for the hydrogen evolution reaction (HER) relative to δ -MoN, a result ascribed to both the presence of octahedral Mo environments and the elevated valence of Mo (+3.4) relative to that of MoN (+3).¹⁴ Using neutron diffraction and pair distribution function (PDF) data, it was demonstrated that Co_{0.6}Mo_{1.4}N₂ crystallizes in the same $1 \times 1 \times 4$ superstructure of δ_1 -MoN as Fe_{0.8}Mo_{1.2}N₂. From these high-quality diffraction data, it was seen that octahedral layers contain only 3+ Mo cations, while prismatic layers have a mixture of 3+ and 4+ Mo. This arrangement is fully consistent with expectations based on ligand field predictions, which additionally cast doubt on the

validity of the δ_1 structure for stoichiometric MoN since the d³ configuration of Mo³⁺ is better stabilized by octahedral than prismatic environments. When this is considered together with the weak sensitivity of prior XRD data to nitrogen positions, the need for definitive structural studies of molybdenum nitride compounds is further highlighted.

It is therefore of great interest to carry out both neutron diffraction and electrochemical studies on a series of close-packed hexagonal molybdenum nitrides to determine which Mo environments and oxidation states are present and to correlate the structural data with electrochemical data to understand the structural and chemical factors that are most responsible for the ORR electrocatalytic activity in this family of compounds. A variety of monometallic molybdenum nitrides were synthesized and electrochemically characterized to gain insights in this regard. The bimetallic molybdenum nitride Co_{0.6}Mo_{1.4}N₂ was also evaluated for its ORR activity, as the incorporation of 3d transition metals is a well-known strategy for potentially improving catalytic activity.⁵

EXPERIMENTAL SECTION

Synthesis. A series of bulk molybdenum nitride samples were prepared by the ammonolysis of different molybdenum precursors at elevated temperatures, following the procedures previously reported to result in products of Mo₂N, δ -MoN, and Mo₃N₆ (Supporting Information, Table S1).¹¹ Co_{0.6}Mo_{1.4}N₂ was synthesized by a two-step solid-state synthesis procedure.¹⁵ Amorphous CoMoO₄ was first prepared by dropwise addition of 20 mL (0.165 M) of CoCl₂ (Alfa Aesar, 99.7%) solution into 10 mL (0.333 M) of Na₂MoO₄ (Alfa Aesar, 95%) solution. The resulting purple precipitate was filtered, dried, and used as precursor for the synthesis of Co₃Mo₃N. Co₃Mo₃N was prepared by reaction under an ammonia atmosphere generated from either a gaseous (flowing NH₃) or a solid (urea with flowing Ar) source, with the reaction products therefore denoted as Co₃Mo₃N and Co₃Mo₃N(s), respectively. The final product Co_{0.6}Mo_{1.4}N₂ was synthesized by annealing Co₃Mo₃N at 400 °C under flowing NH₃.

Characterization. X-ray powder diffraction (XRD) data were obtained using a D8 Advance X-ray diffractometer (Bruker, AXS, $\lambda = 1.54$ Å) with a LynxEye detector set at a diffractometer radius of 300 mm in a Bragg–Brentano configuration. Rietveld refinement scans were collected using a fixed divergence slit width of 0.6°, a 2θ range of 7 to 120°, and a collection time of 1.5 s per step. Time-of-flight (TOF) neutron diffraction measurements were performed on the nanoscale-ordered materials diffractometer (NOMAD) at the Spallation Neutron Source (SNS), Oak Ridge National Laboratory. Powder samples (~100 mg) were loaded into a fused quartz capillary (2 mm diameter), and a data acquisition time of ~100 min was used, achieving a total proton charge of 5.4×10^{12} . Both neutron diffraction and neutron pair distribution function (NPDF) data were processed using the IDL software developed for NOMAD instrument. High-resolution synchrotron diffraction data were collected at beamline 11-BM ($\lambda = 0.413832$ Å) of the Advanced Photon Source (APS) at Argonne National Laboratory 0.8 mm diameter Kapton capillaries. The TOPAS software package (v4.2, Bruker AXS) was used for Le Bail and Rietveld refinements of X-ray and neutron diffraction data.

Electron Microscopy. Scanning electron microscopy (SEM) analysis was carried out on a JEOL 7600F high-resolution microscope with an energy-dispersive X-ray spectroscopy (EDX). Compositional analysis by EDX was done using data collected over an energy range of 0 to 15 keV. Transmission electron microscopy (TEM) was performed on a JEOL 1400 microscope operated at an accelerating voltage of 120 kV.

Electrochemical Testing. Catalyst inks for electrochemical testing were prepared by adding a mixture of 2 mg of nitride sample and 2 mg of carbon black (Vulcan XC72) to a solution of 500 μ L of Milli-Q water, 500 μ L of isopropyl alcohol (70% v/v, Aldrich), and 50 μ L of Nafion-117 (5 wt %, Aldrich) and then sonicating for 30 min to

disperse the catalysts in the ink. Afterward, 25 μL of fresh catalyst ink were dropped onto a glassy carbon (GC) disk electrode (0.196 cm^2 geometrical area, Pine Research Instrument) and dried at room temperature. All electrochemical measurements were conducted in a three-electrode conventional glass cell with an electrolyte solution of 0.1 M HClO_4 . Ag/AgCl was used as reference electrode, and Pt foil was used as auxiliary electrode. Both cyclic voltammetry (CV) and rotating disc electrode (RDE) measurements were performed by sweeping from 0.05 to 1.0 V versus RHE at a scan rate of 10 mV/s. CVs were recorded in solutions saturated with either Ar or O_2 gas. RDE measurements were collected in O_2 -saturated solutions with a rotational speed of 1600 rpm. Durability tests were conducted in air-saturated 0.1 M HClO_4 from 0.05 to 0.8 V versus RHE at a scan rate of 100 mV/s for 2000 cycles. The Koutecky–Levich equation was used to determine the number of transferred electrons during the oxygen reduction reaction. This equation is expressed as $1/j = 1/j_k + 1/(B\omega^{1/2})$, where $B = 0.62nFC_{\text{O}_2}D^{2/3}\nu^{-1/6}$, j is the measured disk current density, j_k is the kinetic current density, ω is the rotation speed, n is the electron-transfer number, F is the faraday constant, C_{O_2} is the concentration of dissolved oxygen in electrolyte, D is the diffusion coefficient of dissolved oxygen, and ν is the kinematic viscosity of the electrolyte.

RESULTS AND DISCUSSION

Phase Identification and Morphology. Structural studies that resolve the bulk coordination environment and oxidation state of cations in the monometallic and bimetallic nitrides are desirable, as these two parameters can strongly impact catalytic activity. We have recently shown that the apparent crystal structure of $\text{Co}_{0.6}\text{Mo}_{1.4}\text{N}_2$ deduced from laboratory XRD data is incorrect and have demonstrated that neutron diffraction data give far better sensitivity to the positions of nitrogen anions, which are in many cases the only atoms whose positions differ between different hexagonal nitride structural variants. In light of these results, we used neutron powder diffraction data to reinvestigate the crystal structures of samples nominally assigned as $\delta\text{-MoN}$, Mo_5N_6 , and $\gamma\text{-Mo}_2\text{N}$ (based on previously reported synthesis procedures).

An initial comparison of the laboratory XRD diffraction patterns of $\delta\text{-MoN}$, Mo_5N_6 and $\gamma\text{-Mo}_2\text{N}$ is provided in Figure 1, though a more detailed structural analysis was also carried

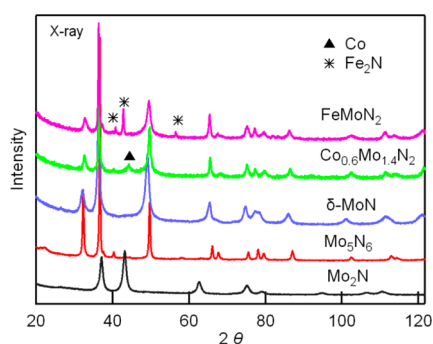


Figure 1. Laboratory XRD patterns ($\text{Cu K}\alpha$) of Mo_2N , Mo_5N_6 , $\delta\text{-MoN}$, $\text{Co}_{0.6}\text{Mo}_{1.4}\text{N}_2$, and FeMoN_2 , with positions of the most intense impurity peaks marked.

out for each phase using synchrotron and neutron diffraction data as described in the subsequent sections. Mo_2N is unique among these compounds in having a cubic lattice. The other compounds have atom positions that are related to the simplest hexagonal lattice subcell expected for close-packed nitrides ($a \approx 2.85$ Å; $c \approx 2.75$ Å), as seen in the strong diffraction peaks at the positions predicted by this subcell. Significant peak

broadening of diffraction peaks is observed for all of the present nitrides, with whole-pattern fitting indicating substantial contributions from both size and strain broadening. The calculated X-ray coherence lengths (which may correspond to crystallite size) were small for Mo_2N (28 nm), $\delta\text{-MoN}$ (34 nm), $\text{Co}_{0.6}\text{Mo}_{1.4}\text{N}_2$ (28 nm), and FeMoN_2 (37 nm). Somewhat larger sizes were seen for Mo_5N_6 (68 nm).

More direct insights into particle size and morphology can be obtained through scanning (Figure 2) and transmission (Supporting Information, Figure S1) electron microscopy studies. It is in general expected that sample morphology will influence electrocatalytic activity of heterogeneous catalysts, since catalytic reactions occur only at the catalyst surface where reactants can bind and products can be released. As can be seen from the SEM data, cubic $\gamma\text{-Mo}_2\text{N}$ exhibits modest sizes of secondary particles with typical diameters of 0.2 to 1 μm . A more lamellar morphology is seen for Mo_5N_6 , which appears to have primary particles up to ~ 1 μm across and secondary particle sizes that are substantially larger. The large particle size of this system may limit catalytic activity. The micron-scale Mo_5N_6 morphology mimics the morphology of the MoS_2 precursor used to prepare the sample, and the substantially nanoscale X-ray coherence length (68 nm) suggests that the resulting Mo_5N_6 particles are strongly polycrystalline. As such, it is expected that synthesis routes recently developed for preparing nanostructured MoS_2 could be adapted to prepare Mo_5N_6 with smaller particle sizes that are more suitable for electrocatalysis applications.^{18,19} A variety of irregular morphologies, including platelike and ellipsoidal crystallites, exist in preparations of $\delta\text{-MoN}$. Among the present nitrides studied, the particle morphologies are most favorable for the bimetallic nitrides $\text{Co}_{0.6}\text{Mo}_{1.4}\text{N}_2$ and FeMoN_2 , both of which formed well-defined spherical crystallites ~ 100 nm in diameter, though there is some evidence of the sintering or fusing of these particles.

While SEM is useful to evaluate the homogeneity of samples on a large scale, TEM analysis was also performed to study morphologies on a smaller scale. TEM images were collected for smaller crystallites ranging from 10 to 150 nm in size (Supporting Information, Figure S1). The anisotropy of the Mo_5N_6 platelets can be clearly resolved, and a common particle size was 150 nm in width and 30 nm in thickness, consistent with the refined XRD coherence length. The primary particle size for $\text{Co}_{0.6}\text{Mo}_{1.4}\text{N}_2$ was typically 50–80 nm, indicating even smaller nanoscale dimensions, which are very suitable for electrocatalysis applications.

Mo_2N Structure. Among these four compounds, Mo_2N has the simplest lattice, and it can be indexed with a small fcc cubic unit cell with $a = 4.1924$ Å based on the refinement of laboratory X-ray data. These small cell parameters result in only a handful of diffraction peaks being observed in laboratory XRD data. To have a sufficient number of peaks to allow the accurate determination of crystallographic parameters from Rietveld refinement, the structural analysis was carried out either using TOF neutron diffraction data from the NOMAD beamline or high-energy synchrotron data from the 11-BM beamline. The positions of the observed diffraction peaks are very similar in the X-ray (Figure 3) and neutron diffraction data (Supporting Information, Figure S2), though the relative peak intensities are very different due to the neutron coherent scattering lengths giving rise to stronger scattering from N ($b = 9.36$ fm) than from Mo ($b = 6.715$ fm). When the Mo occupancy was freely refined using the neutron diffraction data, a stoichiometry of

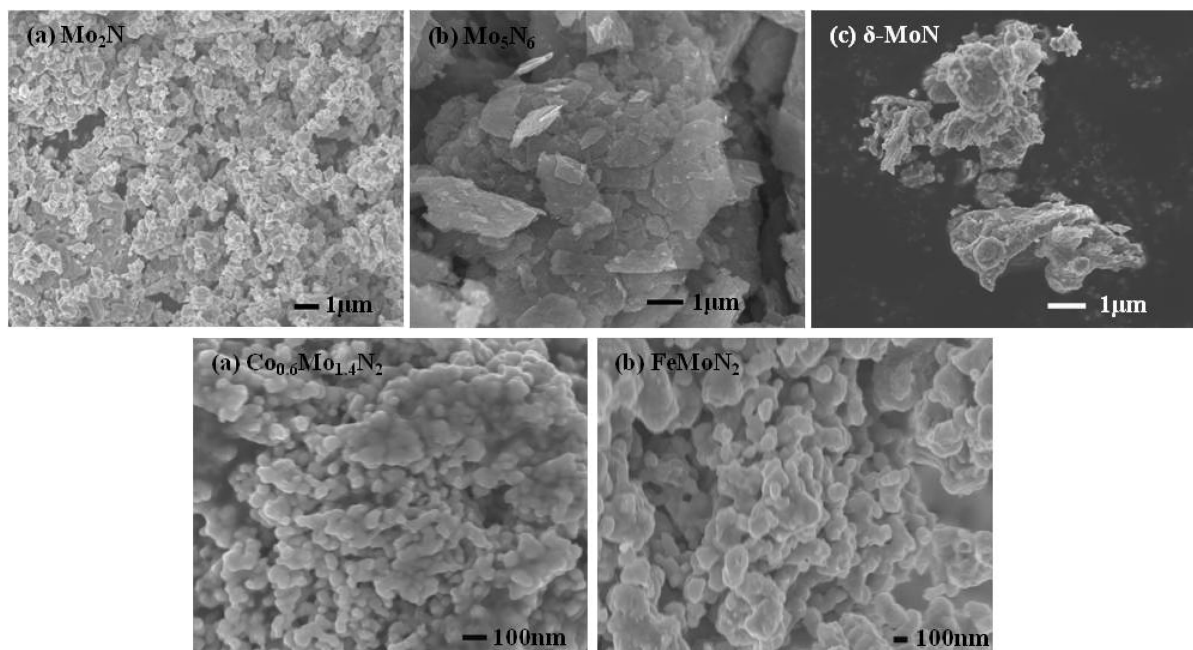


Figure 2. SEM images of nitrides, including (a) Mo_2N , (b) Mo_5N_6 , (c) $\delta\text{-MoN}$, (d) $\text{Co}_{0.6}\text{Mo}_{1.4}\text{N}_2$, and (e) FeMoN_2 . Scale bar is $1\ \mu\text{m}$ for the binary compounds (top) and $100\ \text{nm}$ for the ternary compounds (bottom).

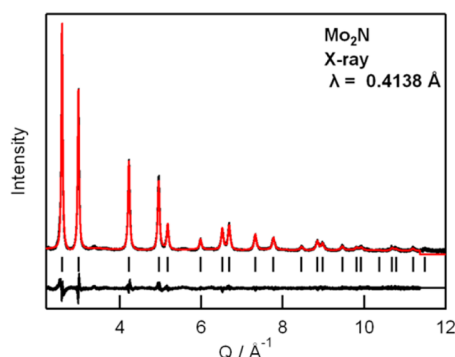


Figure 3. Rietveld refinement data of Mo_2N using synchrotron X-ray data ($\lambda = 0.4138\ \text{\AA}$). The black line indicates the observed data, the red line indicates the calculated data, and the lower black line indicates the difference curve.

$\text{MoN}_{0.534(4)}$ was obtained. This is very near to the ideal stoichiometry of Mo_2N that has been previously proposed and fortuitously suppresses the intensity of the neutron diffraction peaks with the body centered condition of $h + k + l = 2n + 1$ due to the nearly identical scattering power of the cation and anion sites, in a manner similar to the well-known example of KCl.

Despite the consistency of the refined and expected stoichiometry, there are other indications that ideal stoichiometry of Mo_2N may be an imperfect description for this compound. Although X-ray diffraction data are less sensitive to the nitrogen content, the refinement of 11-BM synchrotron data ($\text{MoN}_{0.793(6)}$) suggests that the anion content differs from the ideal stoichiometry. The difference in the refined stoichiometries could potentially be attributed to the anion site containing a mixture of oxygen and nitrogen, which would result in the neutron refinement underestimating the anion site occupancy when the site is refined as only containing nitrogen. Previous studies demonstrated that ammonolysis of MoO_3

produced molybdenum oxynitride.¹⁷ Our initial efforts to use electron microscopy techniques (SEM-EDX, TEM-EELS) were inconclusive in identifying the incorporation of oxygen into the crystal structure of this phase.

Additionally, the background of the neutron diffraction data exhibits a shape characteristic for incoherent scattering, which is interpreted as originating from hydrogen in this sample. Typically, ammonolysis reactions can incorporate hydrogen in a ceramic lattice in the form of either NH_4^+ cations or as complex anions (OH^- , NH_2^- , etc.). The latter is judged more likely, as NH_4^+ typically occupies sites suitable for large cations such as Na^+ or K^+ , and there are no large sites of this type in the simple rock salt structure type of $\gamma\text{-Mo}_2\text{N}$. An examination of the Fourier difference map of the neutron diffraction data showed no discrete peaks in the difference map that might be linked to hydrogen, though if the amount of hydrogen is small and/or if the hydrogens are distributed over a number of symmetry-related positions, it is not expected that the present data would be sufficient to resolve sites of this type. While the present preliminary studies clearly identify the potential crystallographic complexities associated with $\gamma\text{-Mo}_2\text{N}$, more thorough follow-up studies are required to achieve a complete understanding of this phase.

$\delta\text{-MoN}$ Structure. In contrast to Mo_2N , the XRD and neutron diffraction patterns of $\delta\text{-MoN}$ exhibit different lattice periodicities, indicating that the existence of a nitrogen-based superstructure that is essentially invisible to X-rays (Figure 4). While the XRD data for $\delta\text{-MoN}$ can be indexed and refined using a WC-type structural model ($a = 2.857\ \text{\AA}$; $c = 2.805\ \text{\AA}$),¹¹ the neutron diffraction data exhibit strong superstructure peaks that were best indexed with a supercell of $a = 2.857\ \text{\AA}$ and $c = 11.173\ \text{\AA}$ and indicate that the true structure of $\delta\text{-MoN}$ is substantially different from that of WC. The neutron diffraction data could be most effectively modeled using the same space group ($P6_3/mmc$, No. 194) and cation and anion positions as those of $\text{Co}_{0.6}\text{Mo}_{1.4}\text{N}_2$.¹⁴ This $1 \times 1 \times 4$ supercell is generated by an alternative stacking sequence of MoN_6 trigonal prisms

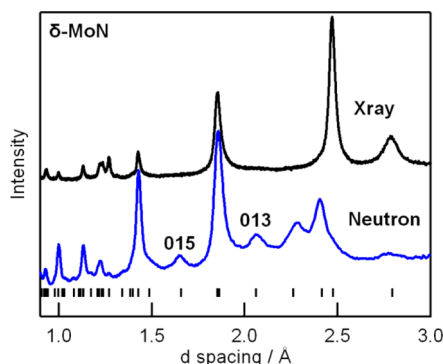


Figure 4. Comparison of X-ray and neutron powder diffraction patterns of δ -MoN in the same d spacing range of 1 to 3 Å. Superstructure peaks such as the marked 013 and 015 reflections are only clearly resolvable in the neutron diffraction data.

and octahedra. Although most peaks of δ -MoN can be well-fit by this four-layered structural model, there is one peak at $d = 2.26$ Å that cannot be described within this structural model. This extra peak may correspond to a minor fraction of a different nitride phase or a different stacking sequence, though these possibilities cannot be effectively distinguished from a single diffraction peak. It is expected that improved synthesis routes can be developed that lead to more homogeneous samples when a technique sensitive to the nitrogen positions (neutron diffraction, Raman spectroscopy, etc.) is used to provide guidance.

Mo₅N₆ Structure. It has been previously reported that Mo₅N₆ also has a four-layered stacking structure. Both X-ray and electron diffraction data suggest that this phase also has a $\sqrt{3} \times \sqrt{3}$ superstructure in the ab plane relative to the simpler WC structure type.^{11,12} The structure previously proposed for Mo₅N₆ has alternating layers of octahedral and prismatic sites like δ -MoN and Co_{0.6}Mo_{1.4}N₂, with Mo vacancy occurring on a prismatic site. However, this literature structure was refined with five independent Mo sites in the proposed space group of $P6_3/m$ (No. 176), which hints that a nonoptimal space group may have been chosen in the course of the analysis of the laboratory powder XRD data used in the initial structure determination study. Our laboratory X-ray data (Figure 1) also showed clear evidence of the c -axis superstructure (including a strong and sharp 002 peak at $d = 5.53$ Å). However, there are only two or three broad peaks associated with the in-plane $\sqrt{3} \times \sqrt{3}$ superstructure (marked with asterisks in Figure 5) suggesting that the in-plane coherence of the superstructure may be limited. The sensitivity of XRD methods to the supercell suggests that Mo cations are involved in the superstructure formation, as may also be inferred by the Mo-deficient (relative to MoN) stoichiometry of this phase.

The synchrotron and neutron diffraction data were first analyzed using the same structural model as Co_{0.6}Mo_{1.4}N₂ ($1 \times 1 \times 4$ superstructure), ignoring the weak in-plane supercell reflections (Figure 5, Supporting Information, Figure S3 and Table S4). The Rietveld refinement of neutron diffraction data using this structural model was quite successful in modeling the observed diffraction peak intensities, and the resulting structural model has both reasonable bond distances and displacement parameters. The occupancies of the trigonal prismatic (1.00) and octahedral (0.70) Mo sites could be clearly seen to be different though the Mo vacancy was found on the octahedral rather than the prismatic site, in contrast to the previously

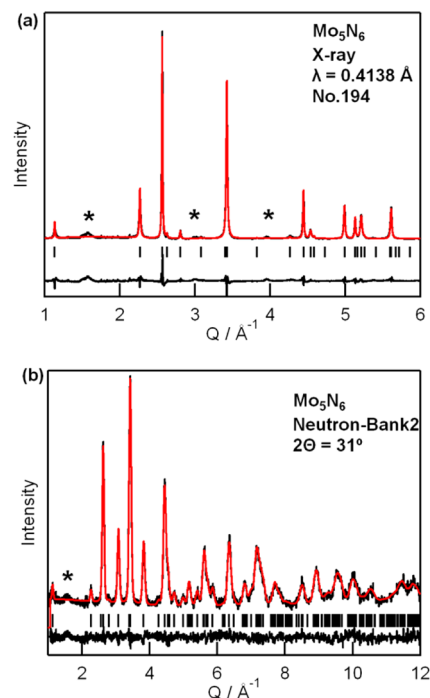


Figure 5. Rietveld refinement profiles for Mo₅N₆ using a $1 \times 1 \times 4$ superstructure of WC in space group $P6_3/mmc$ (No. 194). (a) Synchrotron X-ray data ($\lambda = 0.4138$ Å). (b) Neutron TOF data from bank 2 ($2\theta = 31^\circ$). For the Rietveld refinement, a difference curve (thin black line) is shown below the observed (red) and calculated (black) intensities and marks of reflection positions.

proposed structure. Since knowledge of the N positions is required to correctly differentiate between the prismatic and octahedral sites, the octahedral location of the Mo vacancy determined from the neutron data should be considered definitive.

Efforts to explicitly model the Mo₅N₆ structure using the full $\sqrt{3} \times \sqrt{3}$ superstructure were also carried out. It is difficult to carry out space group determination using powder diffraction data. A search for higher symmetry based on the previously proposed Mo₅N₆ structure indicated space group $P6_3/mcm$ (No. 193) as a plausible alternative. In this space group, a much smaller number of Wyckoff sites can completely describe the atom positions than for the previously proposed structure based on XRD data. In this putative $P6_3/mcm$ space group description, N resides at the 12k site, and Mo is at 2a (prismatic), 4c (prismatic), and 4d (octahedral) sites. This structural model was equally effective at modeling the subcell diffraction peaks in the neutron diffraction data and could also fit the intensity of the weak superstructure peaks once an appropriate model for peak broadening of the superstructure peaks was introduced. Further studies investigating the relationship between synthesis conditions and crystal structure are still merited, and a comprehensive understanding of this structure will require additional synthetic and structural studies that are beyond the scope of the present work.

Co_{0.6}Mo_{1.4}N₂ Structure. As determined from the X-ray and neutron diffraction data (Figure 6), Co_{0.6}Mo_{1.4}N₂ has a $P6_3/mmc$ (No. 194) symmetry hexagonal structure that corresponds to a $1 \times 1 \times 4$ superstructure of WC with alternating layers of octahedral and trigonal prismatic environments, though the x and y coordinates of the cations are identical in both types of layers. Some cobalt metal is present as an impurity phase due to

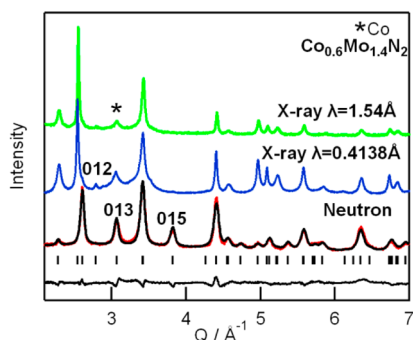


Figure 6. Powder diffraction patterns of $\text{Co}_{0.6}\text{Mo}_{1.4}\text{N}_2$ in the Q range of 2 to 7 \AA^{-1} ($Q = 2\pi/d$), including lab X-ray ($\lambda = 1.54 \text{ \AA}$), synchrotron X-ray ($\lambda = 0.4138 \text{ \AA}$), and time-of-flight neutron data. The impurity peak of cobalt metal is indicated by the asterisk in lab X-ray data. For the neutron Rietveld refinement, a difference curve (thin black line) is shown below the observed (red) and calculated (black) intensities.

the strongly reducing synthesis conditions. Similar to $\text{Fe}_{0.8}\text{Mo}_{1.2}\text{N}_2$,¹³ only Mo is found in trigonal prisms, while both Co and Mo are found in octahedral layers. While octahedral Mo cations have a Mo–N bond distance of 2.17 \AA that is expected for 3+ Mo cations,^{11,13} the shorter (2.12 \AA) prismatic bond distances reflect the higher valence of Mo cations on these sites, with an average prismatic oxidation state +3.6 inferred from the overall stoichiometry.

Local Structure by Pair Distribution Function. Given the complexities observed in the analysis of the bulk structures, the local structures of these nitrides were also investigated. The pair distribution function (PDF) data obtained from the Fourier transformation of the total scattering data diffraction provide direct space insight into bond length distributions that is less sensitive to uncertainties in space group or supercell assignments. The neutron PDF data for the binary nitrides are compared in Figure 7. Clearly, the PDF peaks are substantially

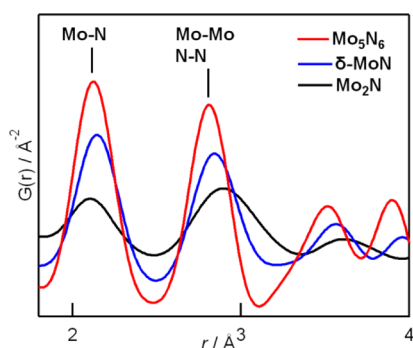


Figure 7. Overlay of neutron PDF patterns of Mo_2N , Mo_5N_6 , $\delta\text{-MoN}$ in the range of 1.7 to 4 \AA .

broad in Mo_2N than in the other two binary nitrides. This is consistent with the relatively large displacement parameters seen for both the Mo and N sites in the Rietveld refinement of the Bragg diffraction data, and is not unexpected due to the presence of crystallographic sites that are only partially occupied. This wide distribution is attributed to the inhomogeneous local environments, as on average only three of the six nitrogen nearest neighbors sites around each Mo cation are occupied, and vacancies are distributed in a random manner judging from the very simple average structure

observed for this compound. The average Mo–N distance in Mo_2N is found to be 2.095(1) \AA based on the PDF refinements. This is shorter than that in other binary nitrides despite the larger ionic radius expected for the low valence Mo (+1.5) ions in this structure. The reduced bond lengths are a consequence of the reduced coordination number of Mo, which will lead to stronger bond for a given cation valence since each bond will be contributing a larger fraction of the total valence.

From the PDF data, it can be seen that the local atomic environments in $\delta\text{-MoN}$ and Mo_5N_6 are qualitatively similar to each other but are different from that of Mo_2N . The Mo–N and Mo–Mo bond distances are slightly shorter in Mo_5N_6 , consistent with the higher average Mo oxidation state in Mo_5N_6 . The PDF patterns of these two phases are otherwise very similar when the short-range correlations (Figure 7) or long-range correlations (Supporting Information, Figure S4) are compared. In both cases, the average structural model used for Rietveld refinements was also effective for modeling the observed PDF data.

An overall comparison of the subcell lattice parameters and the bond distances obtained from PDF refinements for the monometallic hexagonal molybdenum nitrides $\delta\text{-MoN}$ and Mo_5N_6 and the bimetallic molybdenum nitride $\text{Co}_{0.6}\text{Mo}_{1.4}\text{N}_2$ is provided in Table 1. The two compounds with more highly

Table 1. Mo Nitride Subcell Dimensions and Bond Distances Obtained from Neutron PDF^a

in \AA	$\delta\text{-MoN}$	$\text{Co}_{0.6}\text{Mo}_{1.4}\text{N}_2$	Mo_5N_6
a_{sub}	2.865	2.851	2.827
c_{sub}	2.802	2.752	2.767
V_{sub}	19.92	19.37	19.15
Mo–N (oct)	2.183(4) Mo 3+	2.171(6) Mo 3+	2.177(3) Mo 3+
Mo–N (prism)	2.151(3) Mo 3+	2.120(5) Mo 3.6+	2.103(2) Mo 4+

^aFurther details are available in Supporting Information, Tables S5–S8. Nominal site valences are based on the stoichiometry.

oxidized Mo cations both have reduced cell volumes relative to $\delta\text{-MoN}$, though this reduction occurs primarily along the c -axis for $\text{Co}_{0.6}\text{Mo}_{1.4}\text{N}_2$ but is relatively evenly distributed across the a - and c -axes of Mo_5N_6 . In all cases, the octahedral site Mo–N bonds are 2.17–2.18 \AA in length, corresponding to only 3+ Mo at this site. While the prismatic Mo–N bond length remains long for $\delta\text{-MoN}$, this distance is reduced to $\sim 2.10 \text{ \AA}$ in both Mo_5N_6 and $\text{Co}_{0.6}\text{Mo}_{1.4}\text{N}_2$, consistent with more highly oxidized Mo being present at this site. Despite the different expected Mo valence on the prismatic site for these two compounds, the prismatic Mo–N bond distances are essentially indistinguishable. It is not known if this reflects uncertainty in the determination of the Mo bond lengths or the Mo valence. Ligand field arguments suggest that the prismatic site strongly prefers to be occupied by Mo^{4+} , though our experimentally redetermined structure of $\delta\text{-MoN}$ certainly strongly supports the conclusion that Mo 3+ can be stabilized on the prismatic site since the Mo–N bonds in this compound are 0.05 \AA longer than that in its more highly oxidized analogues.

Summary of Structural Features Relevant to Electrocatalysis. Mo_2N is unique in having a cubic structure, very low Mo coordination numbers ($\text{CN} = 3$ on average), and a very low average Mo oxidation state of 1.5+. However, the structures of the hexagonal nitrides, $\delta\text{-MoN}$, $\text{Co}_{0.6}\text{Mo}_{1.4}\text{N}_2$, and Mo_5N_6 are much more similar than previously believed, as all three compounds have been demonstrated through a combined

analysis of neutron and synchrotron powder diffraction data to contain a mixture of octahedral (CN = 6) and trigonal prismatic (CN = 6) Mo cation sites. The diffraction patterns of all three of these compounds can be effectively described using space group $P6_3/mmc$ (No. 194), though this may be an approximant space group rather than the true space group of some of these phases. One common aspect of these compounds is that they all contain an octahedral site whose oxidation state is expected to be 3+ based on the very similar Mo–N bond lengths (~ 2.18 Å) observed for all three phases, though it should be noted that the octahedral site in $\text{Co}_{0.6}\text{Mo}_{1.4}\text{N}_2$ is shared by Co^{2+} (60%) and Mo^{3+} (40%) ions.

In contrast, the length of the Mo–N bonds at the trigonal prismatic site differ and decrease with the increasing valence assigned to the Mo cations at this site for $\delta\text{-MoN}$ (3+, 2.15 Å), Mo_5N_6 (3+, 2.12 Å), and $\text{Co}_{0.6}\text{Mo}_{1.4}\text{N}_2$ (4+, 2.10 Å). The inclusion of Co^{2+} in $\text{Co}_{0.6}\text{Mo}_{1.4}\text{N}_2$ appears to enable the full oxidation of prismatic Mo ions to 4+, while the partial vacancy of the octahedral Mo site allows prismatic Mo ions to be partially oxidized (3.6+) in Mo_5N_6 . There are no obvious chemical reasons for why the previously proposed Mo_5N_6 stoichiometry should be stabilized as a line phase, and as such it is likely that the difference between the refined octahedral site occupancy (0.70) and the ideal value (site occupancy of 2/3) is real. Similarly, it is plausible that the phase that we assigned as $\delta\text{-MoN}$ may have a small fraction of Mo vacancies and that the shorter Mo–N bonds (2.15 Å) at this site relative to the trivalent octahedral site (2.18 Å) may be indicative of the slight oxidation of this prismatic Mo site. Such vacancies might occur through the formation of a proper solid solution, but may also be accommodated through the intergrowth of two phases (stoichiometric and Mo-deficient). More detailed synthetic and structural studies are required to distinguish between these possibilities in the future, and atomic-scale data from TEM studies will be particularly useful in this regard.

Finally, powder diffraction studies indicated that the X-ray coherence lengths of Mo_2N (28 nm), $\delta\text{-MoN}$ (34 nm), $\text{Co}_{0.6}\text{Mo}_{1.4}\text{N}_2$ (28 nm) are very similar. A somewhat larger coherence length was observed for Mo_5N_6 (68 nm), though the implied difference in surface areas is small enough that only minor impacts on catalytic performance would be expected. A larger impact might be expected due to the substantially larger size of secondary particles of Mo_5N_6 observed in SEM and TEM studies. The relatively large secondary particle size mainly derives from the choice of precursor (MoS_2) and could be reduced if alternate synthetic pathways for preparing the MoS_2 precursor were followed.

Oxygen Reduction Reaction Activity of Nitride Catalysts. Rotating disc electrode (RDE) measurements of the ORR activities of three polycrystalline samples nominally comprised of $\gamma\text{-Mo}_2\text{N}$, $\delta\text{-MoN}$, and Mo_5N_6 were carried out in an acidic electrolyte (0.1 M HClO_4). **Caution!** Evaporation can lead to the buildup of perchlorate deposits (e.g., in hoods), which can explode when agitated. The current difference of linear sweep voltammetry (LSV) data collected under O_2 -saturated conditions and Ar-saturated conditions is considered to be the ORR current, as illustrated in Supporting Information, Figure S5. The ORR current data (Figure 8) indicated that all three compounds are active electrocatalysts for the ORR, though the activity of the hexagonal phases ($\delta\text{-MoN}$ and Mo_5N_6) was substantially higher than that of the cubic rock salt phase. The diffusion-limiting current density of Mo_2N is only 4 mA/cm^2 ,

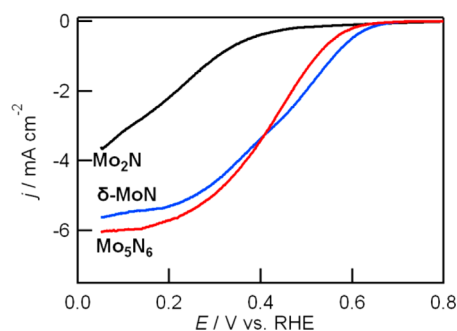


Figure 8. Linear sweep voltammetry data (background-corrected) collected in 0.1 M HClO_4 (1600 rpm).

which indicates that the ORR catalysis pathway for Mo_2N is not a complete $4e^-$ process. In contrast, hexagonal MoN and Mo_5N_6 have diffusion-limiting current densities of 6 mA/cm^2 that correspond to a nearly $4e^-$ O_2 reduction process. It is observed that $\delta\text{-MoN}$ has a slightly higher onset potential than that of Mo_5N_6 , a small difference that might reflect differences in sample morphology rather than differences in intrinsic performance in light of the structural analyses, which indicated that Mo_5N_6 had a larger particle size than the other nitrides.

In addition to testing the ORR activity of monometallic nitrides, the activity of the ternary compounds $\text{Co}_{0.6}\text{Mo}_{1.4}\text{N}_2$ and FeMoN_2 was also evaluated (Figure 9a) under the same solution conditions to determine if a higher oxidation state of Mo or the presence of a redox-active 3d transition metal promotes enhanced catalytic activity. Both $\text{Co}_{0.6}\text{Mo}_{1.4}\text{N}_2$ and FeMoN_2 exhibit substantial ORR activity, though the less active FeMoN_2 compound has a response shifted by ~ 0.10 V more negative. $\text{Co}_{0.6}\text{Mo}_{1.4}\text{N}_2$ is a little more active than $\delta\text{-MoN}$, while FeMoN_2 is a little less active than $\delta\text{-MoN}$ (Figure 9a). The lower activity of FeMoN_2 might in part be due to the presence of a relatively large amount of an impurity phase (Fe_2N), which is likely inactive for ORR, though the magnitude of the shift in ORR response is large enough to suggest that the activity of FeMoN_2 is inherently lower than that of $\text{Co}_{0.6}\text{Mo}_{1.4}\text{N}_2$. Compared to $\delta\text{-MoN}$, the higher oxidation state of Mo (3.4+) in $\text{Co}_{0.6}\text{Mo}_{1.4}\text{N}_2$ is reflected in nonrotating LSV data (Supporting Information, Figure S6, 0 rpm) in the form of a reduction peak at a potential of 0.33 V versus RHE under both Ar and O_2 atmosphere, which is attributed to the reduction of Mo^{4+} to Mo^{3+} .¹⁶ When the activity of $\text{Co}_{0.6}\text{Mo}_{1.4}\text{N}_2$ powders synthesized using gaseous and solid sources of NH_3 are compared, it is found that the use of a solid source results in a qualitatively similar response though with a substantially reduced current (Supporting Information, Figure S7), likely reflecting particle size effects.

The ORR onset potential E_{onset} is for the present work defined as the potential when the current density is 25 $\mu\text{A}/\text{cm}^2$. The E_{onset} value for $\text{Co}_{0.6}\text{Mo}_{1.4}\text{N}_2$ is 0.713 V versus RHE, which is higher than that of $\delta\text{-MoN}$ ($E_{\text{onset}} = 0.680$ V). As can be seen in Figure 9a, $\text{Co}_{0.6}\text{Mo}_{1.4}\text{N}_2$ exhibits a larger current density than isostructural $\delta\text{-MoN}$ at all relevant potentials. As shown in Supporting Information, Figure S8, $\text{Co}_{0.6}\text{Mo}_{1.4}\text{N}_2$ also has a smaller Tafel slope (90 mV/dec) than that of $\delta\text{-MoN}$ (100 mV/dec), which further supports the conclusion that oxygen can be reduced more easily on $\text{Co}_{0.6}\text{Mo}_{1.4}\text{N}_2$ than on monometallic MoN. The enhanced activity of $\text{Co}_{0.6}\text{Mo}_{1.4}\text{N}_2$ relative to MoN may be due to changes in both morphology and the electronic structure induced by Co substitution, though

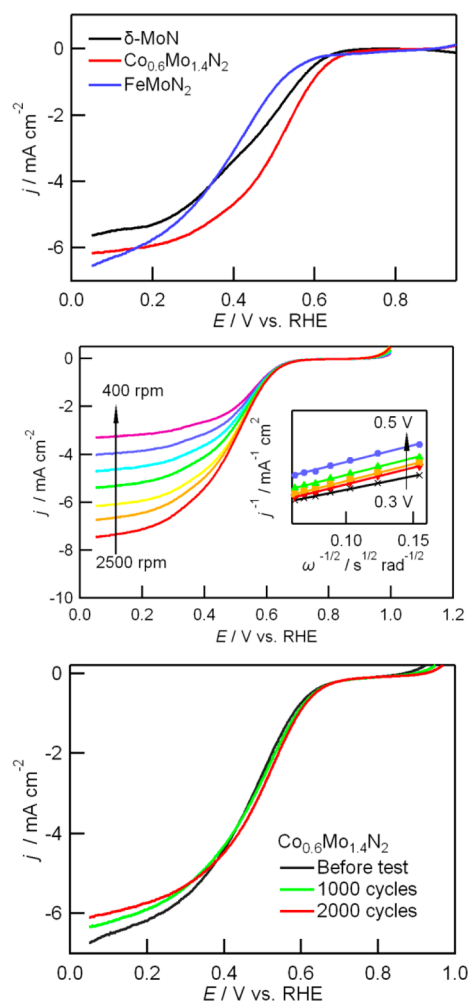


Figure 9. ORR data (background-corrected) collected in 0.1 M HClO_4 . (a) RDE curves of δ -MoN, $\text{Co}_{0.6}\text{Mo}_{1.4}\text{N}_2$, and FeMoN_2 . (b) RDE curves of $\text{Co}_{0.6}\text{Mo}_{1.4}\text{N}_2$ at the rotating speed of 400 to 2500 rpm. (inset) Corresponding Koutecky–Levich plots in the potential range of 0.30 to 0.50 V vs RHE. Additional K–L data are shown in Supporting Information, Figure S9. (c) RDE curves of $\text{Co}_{0.6}\text{Mo}_{1.4}\text{N}_2$ in O_2 before and after durability tests. Durability tests were performed by applying linear potential sweeps (100 mV/s) from 0.05 to 0.8 V vs RHE.

the similar particle sizes inferred from diffraction and electron microscopy studies suggest that electronic structure changes are responsible.

The ORR mechanism of $\text{Co}_{0.6}\text{Mo}_{1.4}\text{N}_2$ was studied by analyzing the rotation rate dependence of RDE data (Figure 9b). Current densities collected at 400 to 2500 rpm were used to determine the number of transferred electrons, n , during the oxygen reduction process through a Koutecky–Levich analysis. Below 0.50 V versus RHE, the value of n obtained in this manner is 4.1, which indicates a four-electron pathway is dominant for ORR in that potential range (the value of n is indistinguishable from the ideal value of 4 within the accuracy of the method). Above 0.50 V versus RHE, oxygen reduction occurs through both two and four electron pathways (the fit value of n is 3.7 at 0.55 V and only 2.3 at 0.6 V, as shown Supporting Information, Figure S9). $\text{Co}_{0.6}\text{Mo}_{1.4}\text{N}_2$ is relatively stable under strongly acidic conditions, unlike most cobalt-containing compounds such as Co metal and CoO, which are easily dissolved in acidic solutions. The electrochemical

capacitance of a $\text{Co}_{0.6}\text{Mo}_{1.4}\text{N}_2$ electrode was slightly reduced after durability testing (Supporting Information, Figure S10), signifying a small decrease in the active surface area of the sample or the dissolution of Co metal originally present in the sample. However, the ORR performance of $\text{Co}_{0.6}\text{Mo}_{1.4}\text{N}_2$ remained high after 2000 cycles, and no large decay was observed (Figure 9c).

When the electrochemical performance of all of the binary and ternary nitrides is evaluated in the context of their structures, some activity trends can be inferred. First of all, it is clear that the hexagonal nitrides appear to be far more active than the cubic nitride Mo_2N . Since Mo_2N differs from the hexagonal nitrides in both its structure and in its much lower Mo oxidation state, it is not possible to judge from the present data which effect has the larger influence on ORR activity, though the latter one is deemed more likely. The variation in activity between the hexagonal nitrides (δ -MoN, Mo_5N_6 , $\text{Co}_{0.6}\text{Mo}_{1.4}\text{N}_2$, FeMoN_2) is surprisingly small, as the response from the different phases does not shift by much more than 0.1 V despite the rather large differences in average Mo oxidation state (3+ to 4+) and chemical composition. For this reason, the ORR activity is tentatively attributed to Mo^{3+} cations in the octahedral site, as this is the one structural feature that appears to be shared by all four of these phases. It should be noted that even though the nominal stoichiometry for the iron phase suggests no octahedral Mo, high-quality diffraction data were unavailable, and it is believed likely that the true stoichiometry of the Fe-containing phase should be expressed as $\text{Fe}_{1-x}\text{Mo}_{1+x}\text{N}_2$ in a manner similar to that of the Co analogue.) As such, it might be expected that the mechanism by which the substitution of Co and Fe tunes the activity of these phases is only by modifying the local environment of the octahedral Mo^{3+} cations, and the induced changes are therefore relatively small. While definitive confirmation of these hypotheses cannot be obtained from the present study due to the limited range of compounds studied, the new structural information obtained through this work suggests that future work involving site-specific substitutions (on just the octahedral or prismatic site) that preserve the Mo oxidation state should be very effective in evaluating these mechanistic hypotheses.

CONCLUSION

The effectiveness of some binary and ternary molybdenum nitrides for ORR electrocatalysis under acidic conditions has been investigated. While cubic rock salt type Mo_2N exhibited poor ORR activity ($E_{\text{onset}} = 0.42$ V), the activities of a variety of hexagonal nitrides (δ -MoN, Mo_5N_6 , FeMoN_2 , and $\text{Co}_{0.6}\text{Mo}_{1.4}\text{N}_2$) were all found to be good with the best performance seen for bimetallic $\text{Co}_{0.6}\text{Mo}_{1.4}\text{N}_2$ ($E_{\text{onset}} = 0.71$ V). Neutron diffraction studies were carried out to have good sensitivity to both cation and anion positions. On the basis of these data, revised structures for both δ -MoN and Mo_5N_6 are proposed in which there are alternating layers of octahedral and trigonal prismatic MoN_6 coordination polyhedra that closely resemble those observed for $\text{Co}_{0.6}\text{Mo}_{1.4}\text{N}_2$. When present, Mo^{4+} cations always preferentially occupy prismatic sites. This structural work clarifies the bonding preferences of Mo cations in nitride structures, and will provide guidance in choosing substitutional strategies for chemical modification that may lead to further improvements in ORR performance. The good ORR activity of these hexagonal nitrides is tentatively attributed to the presence of Mo^{3+} in octahedral coordination, as this is the one structural feature common to the hexagonal nitride phases.

■ ASSOCIATED CONTENT

■ Supporting Information

Synthesis conditions, Rietveld refinement results, and powder diffraction data. This material is available free of charge via the Internet at <http://pubs.acs.org>.

■ AUTHOR INFORMATION

Corresponding Author

*Phone: +1-631-632-7796. E-mail: kpete@bnl.gov.

Funding

Primary funding was provided by the National Science Foundation under the CAREER award DMR-0955646. Acknowledgment is also made to the Donors of the American Chemical Society Petroleum Research Fund for partial support of this research. Additional support was also provided through BNL LDRD 10-0012.

Notes

The authors declare no competing financial interest.

■ ACKNOWLEDGMENTS

This work is supported by Brookhaven National Laboratory under Contract No. DEAC02-98CH10886 with the U.S. Department of Energy, both in the Chemistry Department and in the Center for Functional Nanomaterials user facility. The portion of this research conducted at Oak Ridge National Laboratory's Spallation Neutron Source was sponsored by the U.S. Department of Energy, Office of Basic Energy Sciences.

■ REFERENCES

- (1) Winter, M.; Brodd, R. J. *Chem. Rev.* **2004**, *104*, 4245.
- (2) Gasteiger, H. A.; Kocha, S. S.; Sompalli, B.; Wagner, F. T. *Appl. Catal., B* **2005**, *56*, 9.
- (3) Wang, B. J. *Power Sources* **2005**, *152*, 1.
- (4) Chen, Z.; Higgins, D.; Yu, A.; Zhang, L.; Zhang, J. *Energy Environ. Sci.* **2011**, *4*, 3167.
- (5) Bezerra, C. W. B.; Zhang, L.; Lee, K.; Liu, H.; Marques, A. L. B.; Marques, E. P.; Wang, H.; Zhang, J. *Electrochim. Acta* **2008**, *53*, 4937.
- (6) Avasarala, B.; Murray, T.; Li, W.; Haldar, P. J. *Mater. Chem.* **2009**, *19*, 1803.
- (7) Zhong, H.; Zhang, H.; Liu, G.; Liang, Y.; Hu, J.; Yi, B. *Electrochem. Commun.* **2006**, *8*, 707.
- (8) Xia, D.; Liu, S.; Wang, Z.; Chen, G.; Zhang, L.; Zhang, L.; Hui, S.; Zhang, J. *J. Power Sources* **2008**, *177*, 296.
- (9) Qi, J.; Jiang, L.; Jiang, Q.; Wang, S.; Sun, G. J. *Phys. Chem. C* **2010**, *114*, 18159.
- (10) Bull, C. L.; McMillan, P. F.; Soignard, E.; Leinenweber, K. J. *Solid State Chem.* **2004**, *177*, 1488.
- (11) Ganin, A. Y.; Kienle, L.; Vajenine, G. V. *J. Solid State Chem.* **2006**, *179*, 2339.
- (12) Marchand, R.; Tessier, F.; J. DiSalvo, F. J. *Mater. Chem.* **1999**, *9*, 297.
- (13) Bem, D. S.; Olsen, H. P.; zur Loye, H.-C. *Chem. Mater.* **1995**, *7*, 1824.
- (14) Cao, B.; Veith, G. M.; Neuefeind, J. C.; Adzic, R. R.; Khalifah, P. G. *J. Am. Chem. Soc.* **2013**, *135*, 19186.
- (15) Bhattacharyya, S.; Kurian, S.; Shivaprasad, S. M.; Gajbhiye, N. S. *J. Nanopart. Res.* **2010**, *12*, 1107.
- (16) Pourbaix, M. *Atlas of Electrochemical Equilibria in Aqueous Solutions*; Pergamon Press: Oxford; New York, 1966.
- (17) Sayag, C.; Bugli, G.; Havil, P.; Djéga-Mariadassou, G. *J. Catal.* **1997**, *167*, 372.
- (18) Benck, J. D.; Chen, Z.; Kuritzky, L. Y.; Forman, A. J.; Jaramillo, T. F. *ACS Catal.* **2012**, *2*, 1916.
- (19) Kong, D.; Wang, H.; Cha, J. J.; Pasta, M.; Koski, K. J.; Yao, J.; Cui, Y. *Nano Lett.* **2013**, *13*, 1341.